JGR Space Physics

RESEARCH ARTICLE
10.1029/2023JA031345

Auroral Oval Morphology: Dawn-Dusk Asymmetry Partially Induced by Earth's Rotation

Margot Decotte[1], Karl M. Laundal[1], Spencer M. Hatch[1], and Jone P. Reistad[1]

[1]Department of Physics and Technology, Birkeland Centre for Space Science, University of Bergen, Bergen, Norway

Key Points:

- The auroral occurrence probability (AOP) is derived from Defense Meteorological Satellite Program/Special Sensor J measurements for investigating the auroral oval shape and extent
- The distribution of AOP is persistently larger at dawn than at dusk, regardless of external conditions
- A simple model of plasma sheet magnetic flux indicates that Earth's rotation may contribute to the observed dawn-dusk asymmetry

Correspondence to:
M. Decotte,
margot.decotte@uib.no

Citation:
Decotte, M., Laundal, K. M., Hatch, S. M., & Reistad, J. P. (2023). Auroral oval morphology: Dawn-dusk asymmetry partially induced by Earth's rotation. *Journal of Geophysical Research: Space Physics*, *128*, e2023JA031345. https://doi.org/10.1029/2023JA031345

Received 24 JAN 2023
Accepted 26 MAY 2023

Author Contributions:
Conceptualization: Margot Decotte, Karl M. Laundal, Spencer M. Hatch, Jone P. Reistad
Formal analysis: Margot Decotte
Funding acquisition: Karl M. Laundal
Investigation: Margot Decotte
Methodology: Margot Decotte, Karl M. Laundal, Spencer M. Hatch, Jone P. Reistad
Project Administration: Karl M. Laundal
Supervision: Karl M. Laundal, Spencer M. Hatch, Jone P. Reistad
Writing – original draft: Margot Decotte
Writing – review & editing: Margot Decotte, Karl M. Laundal, Spencer M. Hatch, Jone P. Reistad

Abstract The auroral oval morphology has been investigated in previous studies presenting maps of average auroral precipitation. However, such distributions tend to emphasize auroral intensity rather than the actual extent of the auroral oval. We develop a statistical method to characterize the auroral oval morphology by using 20 years of electron energy flux measurements from the Defense Meteorological Satellite Program/Special Sensor J (DMSP/SSJ); instead of relying on auroral oval boundaries, we derive the probability of observing aurora from a threshold of 2.10^9 eV/cm^2/s/sr above which the total energy flux of electrons (in the energy range 1–30 keV) is defined as aurora. We then investigate the auroral occurrence probability (AOP) in the magnetic latitude-magnetic local time (MLat-MLT) sectors covered by DMSP for various conditions related to geomagnetic activity. Regardless of those conditions, the AOP distributions reveal a width asymmetry with a wider dawn-to-noon sector (06–12 MLT) compared to the dusk-to-midnight sector (18–24 MLT), the dawn preference getting even more pronounced as the geomagnetic activity decreases. In the context of an open magnetosphere, we investigate the relation between the observed extent asymmetry in the auroral oval and the magnetospheric plasma convection. Representing the plasma sheet magnetic flux as a one-dimensional fluid subject to production on the nightside (closing of flux via reconnection) and loss on the dayside (opening of flux), we highlight similarities with the AOP in terms of MLT asymmetries. Finally, making use of this fluid model, we demonstrate that the corotation influence on the plasma convection pattern is consistent with the dawn-dusk asymmetry observed in the AOP distributions.

Plain Language Summary As an indirect consequence of the magnetic interaction between solar wind and Earth, protons and electrons precipitate into the ionized upper atmosphere (ionosphere) at high latitudes. These charged particles can excite atmospheric atoms at approximately 100–200 km altitude, which in turn potentially emit photons in the visible light spectrum during relaxation; this is what we call aurora. However, instruments aboard satellites crossing the polar regions, where aurora take place, can measure particles that will not necessarily result in sharp, visible aurora from the ground. This diffuse aurora represents the largest part of the total auroral energy deposited into the ionosphere. We show that the probability to measure this type of aurora is close to one within an oval-shaped region (auroral oval) around each pole, at all local times (including daytime), independently of geomagnetic conditions. We find a systematic pattern in the statistical extent of the diffuse auroral oval depending on local time, with a larger oval in the dawn region, compared to dusk. We aim at understanding the auroral oval morphology in terms of large-scale magnetospheric plasma dynamics, also including the Earth's rotation influence.

1. Introduction

Since the first reported scientific observations of auroras (Tromholt, 1882), there have been many auroral studies whose observational data from all-sky cameras resulted in the establishment of the auroral oval concept by Feldstein in the 1960s (e.g., review by Y. Feldstein (2016)). Since then, the auroral oval morphology has been investigated in great detail and discussed in connection with variations in the geomagnetic activity (e.g., Y. I. Feldstein, 1964; Feldstein & Starkov, 1967; Holzworth & Meng, 1975). It is now broadly accepted that the region where auroras occur most frequently is an approximately oval-shaped Sun-fixed zone located at high latitudes around the geomagnetic pole; its exact position depending on the solar-terrestrial physics.

Dungey (1961) was the first to put forward the concept of an open magnetosphere to study the interactions between solar wind, magnetosphere, and ionosphere. It has since been extensively demonstrated that the dynamics of the magnetosphere-ionosphere system is controlled by the convection of plasma and magnetic flux (Moore et al., 1989), with the direction and magnitude of the interplanetary magnetic field (IMF) playing a dominant role

(Cowley, 1981). Cowley and Lockwood (1992) later came up with the expanding-contracting polar cap (ECPC) paradigm to describe the ionospheric convection in this context. The ECPC model predicts how the size of the polar cap, which is delimited by the open-closed boundary (OCB), depends on the amount of open magnetic flux in the magnetotail lobes which is in turn controlled by the magnetic reconnection rate. Because of its crucial role in the solar wind-magnetosphere-ionosphere coupling, the OCB has been widely studied over the last decades. The OCB location dependence on season and IMF orientation (Laundal et al., 2010), the derivation of the OCB location from the region 1 to region 2 field-aligned currents boundary (Burrell et al., 2020), and OCB location variations during substorm cycle (Milan et al., 2003) are among such studies. It is now generally accepted that the poleward boundary of the auroral oval and the OCB behaviors and locations are so closely related that they describe the same physical limit (Chisham et al., 2022). This can be seen for instance in the maps of the ionospheric precipitation regions with superposed convection streamlines presented by Newell et al. (2004).

On the other hand, much less is known about how the auroral oval's equatorward boundary behaves in the context of the ECPC paradigm. That there is currently no model or standard technique for predicting where exactly the equatorward boundary lies indicates that what controls the auroral oval spatial distribution is still not fully understood. Furthermore, existing statistical models of the aurora usually concentrate on the average energy flux or brightness of auroral precipitation rather than the extent of the auroral oval (Dombeck et al., 2018; Newell et al., 2009, 2014; Shue et al., 2001). Such models are well suited to explain the statistical behavior of accelerated aurora, which is controlled by kinetic processes such as particle drifts, particle acceleration in the auroral region and wave-particle interactions (Coumans et al., 2002; Newell et al., 2009; Ni et al., 2016). However, these studies give less attention to regions of weak and/or diffuse auroral precipitation. Yet, the diffuse precipitation, caused by electrons originating in the plasma sheet, represents the largest contribution to the total auroral energy precipitating into the ionosphere (Khazanov & Glocer, 2020).

In this study, we use precipitation data from the Defense Meteorological Satellite Program (DMSP), as previously done by Kilcommons et al. (2017) who implemented an auroral boundary identification algorithm to find the auroral oval limits. Here, we instead investigate the auroral occurrence probability (AOP), which allows for including both high and low energy precipitation in our statistics, and we expand the ECPC concept to treat the auroral oval as a mapping of a magnetospheric plasma region to garner new insight of the auroral oval spatial span. As we seek to understand the dominant processes involved in shaping the aurora, we explore the resulting auroral occurrence distributions as a function of external conditions such as geomagnetic activity and substorm phase.

In Section 2, we present the databases used to achieve our study; these include precipitation data as the core data, solar wind magnetic field and plasma data, as well as substorm epochs. In Section 3 we describe our methodology for deriving the AOP from the electron energy flux. In Section 4 we compare the AOP with the average energy flux. We also show maps and magnetic local time (MLT) profiles of the AOP for separate IMF and substorm epoch conditions, as well as for different auroral detection thresholds, and we emphasize an observed recurrent pattern. In Section 5 we provide and discuss a possible interpretation for our observations given a fluid framework in which the auroral oval maps to the plasma sheet magnetic flux, which is in turn influenced by the Earth's rotation. Finally, in Section 6 we summarize the methodology we apply for modeling the auroral oval extent, as well as the main results of this study. A brief statement of future possible work is also included.

2. Data

The database we use comprises about a billion individual electron precipitation spectra together with the corresponding solar wind and geomagnetic conditions. Since this constitutes too much data to fit in memory with standard Python libraries, we use the Vaex library (Breddels & Veljanoski, 2018) to perform our analysis. This library enables fast statistical analyses of the auroral oval morphology based on various data selection criteria. The different sources of data are described in the following subsections.

2.1. DMSP Particle Data Set

Our methodology relies on energy flux measurements of auroral electrons provided by the US Defense Meteorological Satellite Program (DMSP). The DMSP fleet consists of several low Earth-orbiting satellites at altitudes of approximately 830–850 km that are in Sun-synchronous (i.e., fixed in local time, see subsection 3.1), three-axis

stabilized and nearly circular polar orbits approximately in the dawn-dusk meridian plane, with a periodicity of 101 min and an orbital inclination of 98.7°–98.9°. For the purpose of our statistical analysis we use most of the CDAWeb database described in Redmon et al. (2017), that is, a total of 21 years of observations, within the 2000–2014 time period. All measurements are made by the SSJ/4 and SSJ/5 (Special Sensor J) electrostatic analyzer instruments on board nine of the DMSP satellites. By pointing within the downward atmospheric loss cone at auroral latitudes, these detectors measure precipitating particles between 30 eV and 30 keV using 20 energy channels, thus providing a fairly complete energy spectrum of the particles that cause the aurora at 1-s cadence. We provide the spacecraft location in modified Apex coordinates (Richmond, 1995).

2.2. High Resolution OMNI Database

To investigate the solar wind–auroral precipitation coupling, the DMSP precipitating particle data are combined with the multi-source OMNI data set of solar wind magnetic field and plasma parameters compiled from observations made by IMP-8, ACE, Wind, ISEE-3, and Geotail spacecrafts (Papitashvili et al., 2014). The best near-Earth estimates of solar wind properties are obtained by time-shifting upstream observations to represent the conditions at the nose of the Earth's bow shock (King & Papitashvili, 2005). Hence, there are non-negligible uncertainties in the solar wind parameters affecting the magnetosphere (Di Matteo & Sivadas, 2022). We use IMF data and geomagnetic indices provided by the 1-min resolution OMNIWeb database, between 2000 and 2014. From the OMNI database, we use the y (dawn-dusk) and z (north-south) components of the interplanetary magnetic field given in geocentric solar magnetospheric (GSM) coordinates, the ring current SYM-H index, and the auroral electrojet index AL. To temporally align this data of 1-min resolution with the 1-s resolution DMSP data set, we associate each DMSP data point with the OMNI data point from the nearest preceding minute.

2.3. Isolated Substorm Onset List

To determine how the auroral precipitation varies throughout the substorm cycle, we combine the DMSP observations with 13,000 substorm onsets identified from SuperMAG-derived auroral electrojet (SML) indices (Ohtani & Gjerloev, 2020). From the Ohtani and Gjerloev original substorm list, we exclude onsets distinct by less than 2 hr from the nearest onset, to ensure that our analysis focus on isolated substorms. This way, we aim at observing a clean response of the AOP to substorm epochs, without any ambiguity on the possible influence of already ongoing activity. Since isolated substorms tend to be weaker than "recurrent" substorms (Rodger et al., 2016), our statistics may slightly underestimate typical substorm effects. We perform a superposed epoch analysis using all the DMSP data described in Section 2.1.

3. Methodology—Auroral Occurrence Probability

In this section, we introduce the concept of AOP that our study relies on. In particular, we show how this quantity might be more appropriate, given the DMSP orbits, than using auroral boundary identification for our investigation of the extent of the auroral region. We also describe the relevance to our purposes of the choice of parameters (energy range and threshold for aurora detection) on which the AOP is based.

3.1. Local Time Orbital Bias Introduced by Sun-Synchronous Satellites

Each DMSP spacecraft is synchronised such that its orbit is always at the same fixed position relative to the Sun (Sun-synchronous orbit), that is, the spacecraft always visits approximately the same latitude at the same local time; thus the distribution of in situ measurements made by a Sun-synchronous satellite is biased toward particular local times. In this paragraph, we briefly demonstrate how such data can produce a statistically biased estimate of the auroral boundaries. While we point to the DMSP satellites and more generally to satellites in Sun-synchronous orbit, the issue described here remains true on short time periods for non-Sun-synchronous satellites, as long as such a satellite stays in the same local time plane during that time.

Figure 1 shows the simulated trajectory (gray lines in left panels) of a synthetic Sun-synchronous satellite over a period of 1 year in the Northern (top left panel) and Southern (bottom left panel) Hemispheres. The orbital plane of the satellite sweeps over a wide band in magnetic coordinates due to the offset between magnetic and geographic poles—this offset being larger in the Southern Hemisphere. We define an ideal auroral boundary

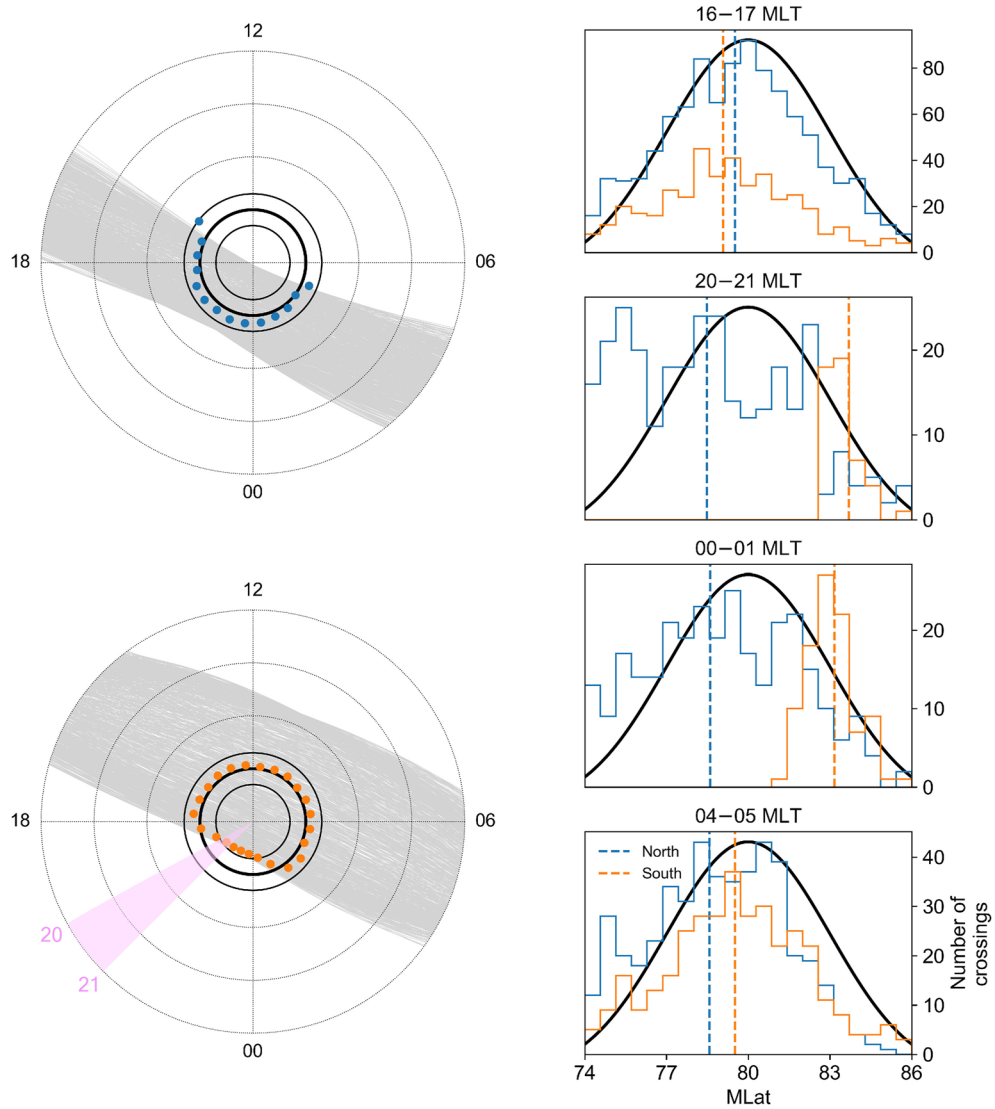

Figure 1. Left: Simulated synthetic Sun-synchronous orbits (gray) during 1 year for the Northern (top) and Southern (bottom) Hemispheres. The latitudinal range spans 50°–90° MLat. The circular black lines indicate the statistical location of the theoretical true auroral boundary, which is modeled as a Gaussian random variable having a mean of 80° MLat (thick line) and a standard deviation of 3° (thin lines at 80° ± 3° MLat). The colored dots indicate the average position of the measured boundary crossings in each covered magnetic local time (MLT) sector. Right: Gaussian and measured distributions of boundary crossings in the Northern (blue) and Southern (orange) Hemispheres for four MLT sectors spanning 1 hr. The dashed vertical line marks the average latitude of the distribution of sampled boundary crossings in each hemisphere.

represented by a Gaussian distribution centered at 80° magnetic latitude (MLat) (thick black line), with a standard deviation of 3° (thin black lines). For each simulated satellite crossing of the polar region, the MLat location of the auroral boundary is sampled from this Gaussian distribution. The resulting MLat distribution of measured boundary crossings can be derived at each MLT for the Northern (blue) and the Southern (orange) Hemispheres, as shown for four different MLT sectors spanning 1 hour at right in Figure 1, together with the correct distribution (in black). The average MLat location of the sampled boundary is shown as a colored dot at each MLT (left panels) and as a vertical colored dashed line for the four 1 hr-MLT sectors (right panels), in both hemispheres. Since the satellite does not measure the full distribution in local time sectors poorly covered by the satellite orbit, the sampled distribution is deformed compared to the correct distribution and, as a consequence, the mean position of the modeled boundary is biased and does not match with the Gaussian's peak at 80°. An obvious example of this is the 20–21 MLT sector in the Southern Hemisphere (highlighted pink region) in which the statistically identified boundary lies several degrees above the actual mean magnetic latitude of the boundary.

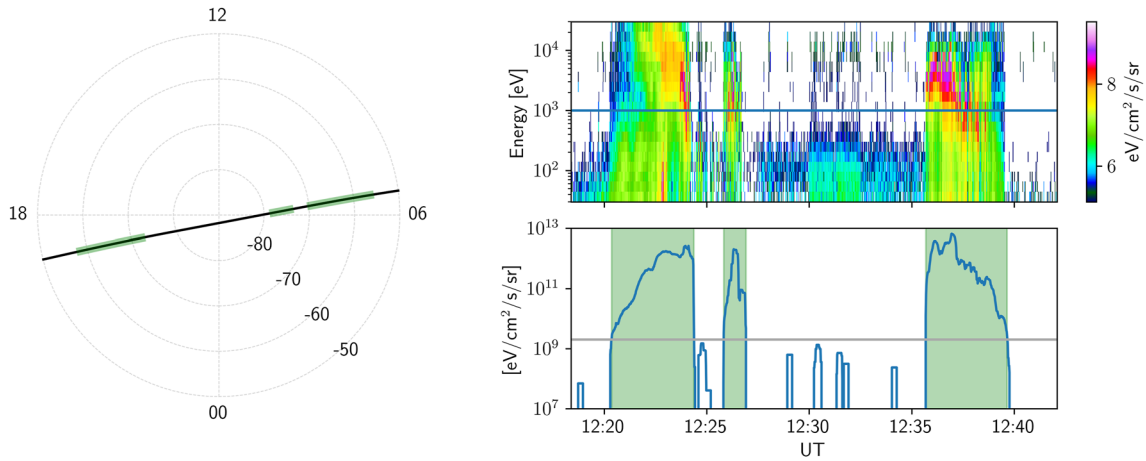

Figure 2. Example auroral identification based on electron precipitation data from one southern polar region crossing by Defense Meteorological Satellite Program (DMSP) F16 on 29 May 2010. Left: The spacecraft orbit is shown in black as Apex magnetic latitude and magnetic local time. Right, top panel: The electron energy spectrogram with the channel energy of the 19 DMSP Special Sensor J channels on the *y*-axis and time on the *x*-axis. The blue horizontal line corresponds to an energy of 1 keV. Bottom panel: The electron energy flux integrated over all of the channels with center energies of at least 1 keV is shown in blue, while the gray horizontal line shows our threshold for auroral detection ($2 \cdot 10^9$ eV/cm^2/s/sr). In this example, the auroral identification algorithm detects three auroral regions, shown shaded in green. The identified auroral regions are also highlighted in green along the satellite orbit (left).

We emphasize that although the local time bias is reduced when using multiple satellite orbits, it persists as long as the MLT coverage is not sufficient. While we combine data from several DMSP satellites in our analysis, we will show in Section 4.2 that some MLT sectors are still poorly covered (see Figure 4); we thus expect the local time bias to be significant in these regions.

Based on these results we conclude that using the Kilcommons et al. (2017) auroral boundary data set derived from the DMSP/SSJ precipitation data would lead to a mistaken analysis in our study of the extent of the auroral oval. We nevertheless base the model of auroral oval presented in this paper on the concept of AOP which relies on several aspects of the work of Kilcommons et al. (2017), as we now discuss in the succeeding subsections.

3.2. Energy Range and Threshold for Detection of Aurora

At the origin of the AOP concept is a binary time series that indicates if a particular loss cone electron energy flux spectrum measured by the DMSP/SSJ instrument constitutes an observation of auroral precipitation. Such binary information is produced by following the method of identification of candidate auroral regions presented in Kilcommons et al. (2017). An example of aurora detection is illustrated in Figure 2, using DMSP/SSJ electron precipitation data from a single satellite pass. The corresponding electron energy spectrogram is shown in the top panel at right. We adopt Kilcommons et al. (2017) choice to classify electron energy spectra as either "aurora" or "non-aurora" based on examination of electron precipitation of at least 1 keV (horizontal blue line). We use the Hardy et al. (1985) technique to integrate the differential electron energy fluxes from the nine highest energy channels of the SSJ instrument, which cover 1.392–30 keV (Redmon et al., 2017). The bottom panel at right in Figure 2 shows the resulting integrated energy flux (in blue) and the threshold of $2 \cdot 10^9$ eV/cm^2/s/sr used for aurora detection (horizontal gray line). Eventually, precipitating electron fluxes exceeding this threshold are deemed "aurora" (shown shaded in green), and "not aurora" otherwise, such that we end up with a Boolean (True/False) value for every DMSP/SSJ electron energy flux data point. Our choice of threshold is similar to the threshold used by Kilcommons et al. (2017) ($1 \cdot 10^9$ eV/cm^2/s/sr), which has been shown to be suitable for the detection of auroral regions that map to the central or boundary plasma sheet (Newell et al., 1996).

For comparison, by assuming an isotropic flux over the loss cone and a solid angle of π, our threshold is equivalently $5 \cdot 10^{-3}$ mW/m^2 which is more than two orders of magnitude below the 1 mW/m^2 auroral brightness that Keiling et al. (2003) define as visible aurora. Thus our threshold for identifying aurora should not necessarily be construed to mean "visible aurora." Additional discussion on our choice of a threshold value, as well as its influence on the auroral oval model that we present, is located in Section 4.3.

3.3. Auroral Occurrence Probability

Once the binary data is generated, each DMSP/SSJ data point is binned into an approximately equal area grid covering 50°–90° MLat with rings of width 1° MLat divided into a varying number of cells, with 2 cells in the most poleward circle (89°−90°) and 68 cells in the most equatorward circle. Bins with less than 200 measurements are discarded to ensure a robust statistical analysis. In each of the remaining MLat-MLT bins, we calculate the probability of observing aurora by dividing the sum of all observations identified as aurora by the total number of measurements. In order to have a suitable way to visualize the auroral oval morphology, especially when it becomes asymmetric, the resulting probabilities are processed in two ways: (a) we display the AOP and the underlying grid on a polar map, and (b) we derive the MLT variation of the AOP. Such an MLT profile is derived by interpolating the gridded probabilities to an MLT-MLat grid with 0.5° resolution in MLat and 8 min resolution in MLT and then averaging the gridded value over latitude. From now on, the resulting quantity is referred to as the 1D-AOP. We point out that, unlike the AOP, the 1D-AOP is no longer a probability, and its unit is arbitrary; nonetheless, it can still be used to study the variation of the probability as a function of MLT. We will see that the auroral occurrence oval exhibits asymmetries that are often more easily detected by way of the 1D-AOP than by looking at the AOP maps, especially when comparing distributions for different conditions.

In addition to eliminating the local time bias present in statistics of auroral boundaries identified from in situ Sun-synchronous satellite measurements (Section 3.1), the AOP allows us to use much more of the entire set of DMSP/SSJ measurements, as we do not lose polar passes for which both the poleward and equatorward boundaries cannot be identified. The AOP moreover includes observations of no or low precipitation rather than discarding the information that they provide. In other words, the AOP makes use of all observations made during every DMSP pass within the auroral zone. We believe that such a data set is ideally suited for investigating the auroral oval morphology.

4. Results

In this section, we first review the similarities and differences between the AOP and the average energy flux. Then we look exclusively at the AOP and we investigate further the maps and MLT profiles resulting from our data analysis. In particular, we explore the response of the auroral occurrence oval morphology to various parameters within our global data set.

4.1. Comparison Between the AOP and the Average Energy Flux

As stated in the introduction, large-scale, long-term studies of the auroral oval have tended to focus on parameters such as the average energy flux. The MLat-MLT distribution of such a quantity mainly reflects high-energy precipitation as it gives more weight to the MLat-MLT bins with high energy flux values over those with lower energy flux. Conversely, the distribution of AOP is based on equally weighted observations within each MLat-MLT bin and is thus better suited to characterize to what degree each bin experiences precipitation.

Figure 3 shows maps of AOP (left) and mean energy flux (right) in the Southern Hemisphere, as derived from our data set for geomagnetically quiet (B_z positive, top) and active (B_z negative, bottom) periods. The post-noon and post-midnight data gaps are the result of the incomplete coverage of these sectors due to the Sun-synchronous orbits of the DMSP spacecraft (see also Section 4.2).

It is worth mentioning that the energy flux distributions introduced here are similar to the diffuse aurora energy flux presented by Newell et al. (2009). In particular, the energy flux pattern for B_z negative is almost indistinguishable from Newell's energy flux for high solar wind driving. For B_z positive, that is, low solar wind driving, our map of energy flux and those of Newell present some differences in the location of intensity peak but are still fairly comparable. On the other hand, we do not have any reference to compare our diffuse aurora probability distributions with since Newell et al. (2009) have only derived the probabilities of observing monoenergetic and broadband aurora in their study.

The comparison between the AOP and the mean energy flux reveals that the auroral oval, as reflected in the AOP, is extended over a wider range of latitudes than the auroral oval reflected in the mean energy flux. This larger auroral oval is expected as the AOP takes into account the weak precipitation, unlike the average energy flux distribution. However, apart from the difference in width, it is apparent that the overall morphologies of the AOP

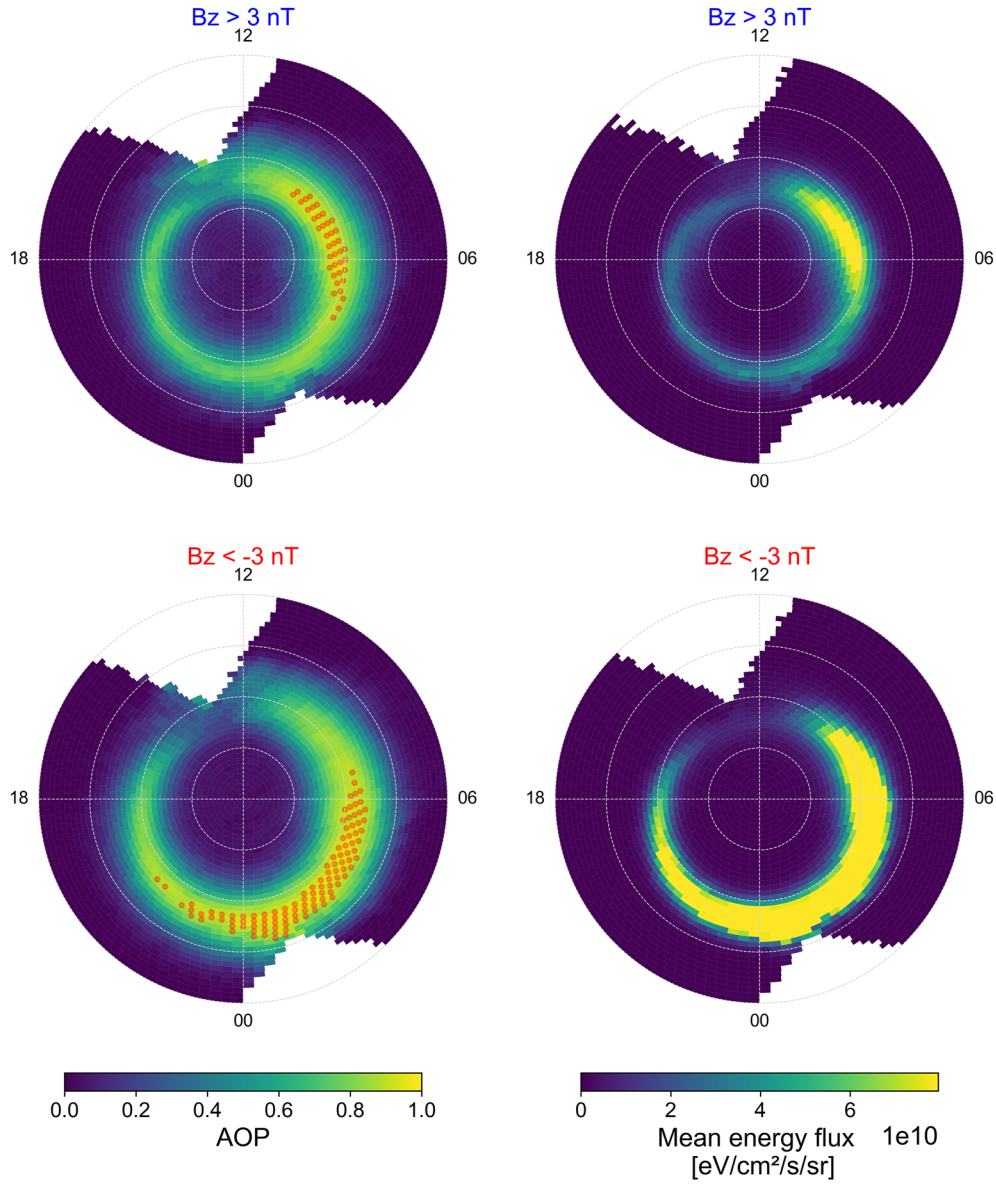

Figure 3. Distributions of auroral occurrence probability (AOP) (left) and mean energy flux (right) for B_z positive (top) and B_z negative (bottom) in the Southern Hemisphere. All distributions presented in this paper span over 50°–90° |MLat|, for all MLTs covered by the orbits of our DMSP satellite selection (see Section 2.1). The red dots on the left maps indicate bins with AOP value > 0.9 (AOP peak).

and the average energy flux are somehow equivalent. In particular, the peak of the AOP distributions (shown as red dots on the left maps), defined by AOP values exceeding 0.9, matches the regions of enhanced mean energy flux. In addition to that, both quantities exhibit a similar asymmetric pattern between dawn and dusk, more or less prominent depending on the geomagnetic conditions, but persistent anyhow. We discuss the shape and extent features of the AOP in more detail in the following section.

4.2. A Dawn-Dusk Asymmetry in the AOP

The top panel of Figure 4 shows the AOP distributions derived from the entire 20-year data set for the Northern (left) and Southern (right) Hemispheres, while the line plot in the bottom panel of Figure 4 shows the corresponding 1D-AOP as a function of MLT (gray and black for the Northern and Southern Hemispheres, respectively). The data gaps seen on the maps (and evoked in the previous section) also appear in the 1D-AOP distributions,

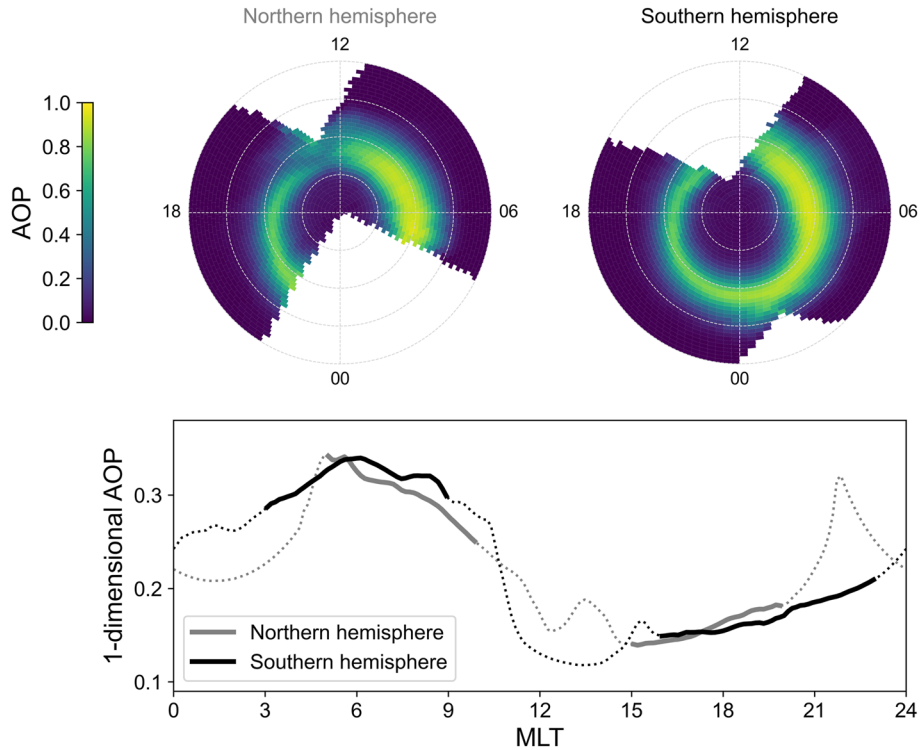

Figure 4. Top row: magnetic latitude-magnetic local time (MLat-MLT) distributions of auroral occurrence probability (AOP) for the Northern (left) and Southern (right) Hemispheres. Bottom panel: 1D-AOP as a function of MLT for the Northern (gray) and Southern (black) Hemispheres. The thick line indicates MLT regions well covered by the satellite orbits, while the thin line corresponds to MLT regions with incomplete coverage.

with dotted (thick) lines indicating MLTs where coverage is insufficient (sufficient) to derive a reliable estimate of the 1D-AOP. It can be seen that the Southern Hemisphere benefits from a better coverage than the Northern Hemisphere due to the larger offset between magnetic and geographic poles in the South. As a consequence, most of the nightside data in the following analysis comes from the Southern hemisphere with a negative tilt angle.

Beyond differences in coverage, there are no major distinctions between the distributions of AOP in the two hemispheres. This is especially clear from the MLT profiles of 1D-AOP which are likewise similar in shape, in fairly covered sectors. Furthermore, it can be seen from covered sectors that both maps exhibit a comparable variation of the AOP with MLT. In particular, the auroral occurrence oval is distinctly wider in the dawn-to-noon sector than in the dusk-to-midnight sector. This dawn-dusk asymmetry can also be seen from the 1D-AOP in both hemispheres.

From now on, considering that the AOP does not meaningfully differ between the two hemispheres, we combine measurements from both hemispheres in order to improve the spatial coverage of the auroral region. Even so, and despite an excellent coverage for most local times between 50° and 60° |MLat|, the very poorly covered postnoon and postmidnight regions below 60° |MLat|exhorts us to be careful when interpreting the upcoming results of our statistical analysis in these MLT sectors. We especially expect that the lack of coverage would affect our results when the auroral occurrence oval lies at low latitudes and/or is particularly wide. On the other hand, the regions 4–11 MLT (~dawn) and 16–23 MLT (~dusk) can be considered with confidence.

4.3. Response of the AOP to the Threshold for Aurora Detection

In Section 3.2 we have briefly introduced the choice of threshold above which integrated high-energy electron energy flux measurements made by DMSP are deemed to be aurora. Here we show how the AOP varies with the choice of threshold, and we explain our final choice in more detail.

Figure 5 shows the AOP distributions (top) and the corresponding MLT profiles of 1D-AOP (bottom), as derived from three thresholds for positive identification of aurora, within an order of magnitude around the value of

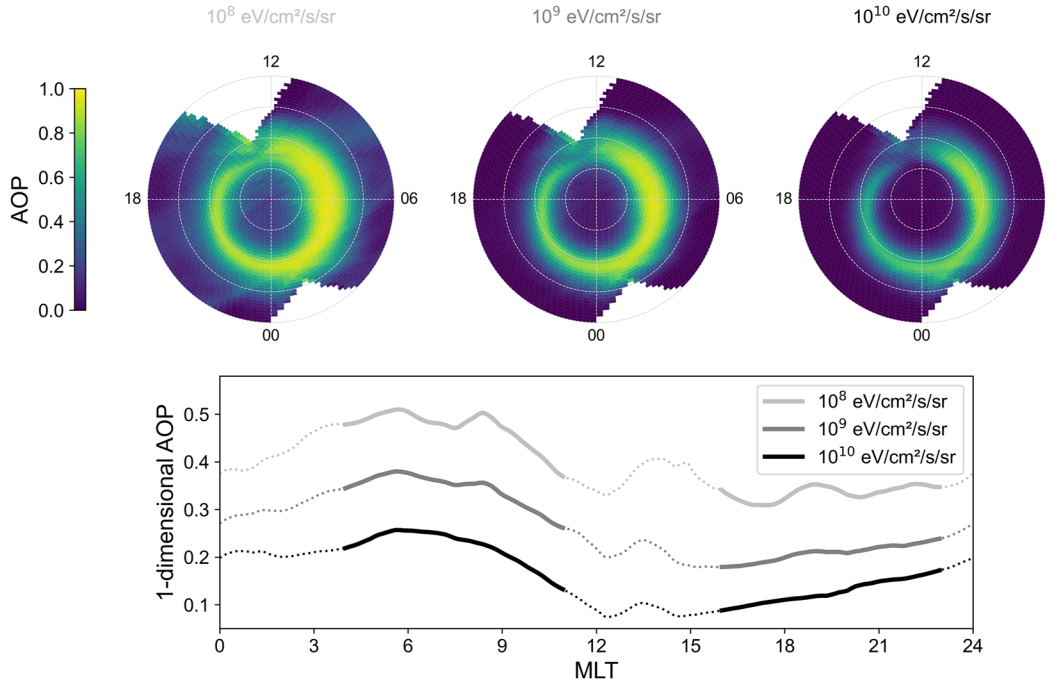

Figure 5. Auroral occurrence probability (AOP) distributions (top row) and magnetic local time profiles of 1D-AOP (bottom panel) for three different thresholds above which integrated high-energy (≥1 keV) electron energy flux is deemed to be aurora. From left to right the threshold values are respectively 10^8 eV/cm^2/s/sr (light gray), 10^9 eV/cm^2/s/sr (gray), and 10^{10} eV/cm^2/s/sr (black). The middle value is also the threshold used in the study of Kilcommons et al. (2017).

$1 \cdot 10^9$ eV/cm^2/s/sr (Kilcommons et al., 2017). The morphology of the AOP distributions is similar for all three thresholds, especially the dawn-dusk asymmetry and the overall preference for the dawn side, as already described in the previous section. However, the choice of different thresholds results in auroral occurrence ovals with varying intensities; in particular, a lower threshold for aurora detection yields a more intense auroral oval, with a higher probability of observing aurora everywhere in the auroral zone, compared to a higher threshold. In addition, a decreased threshold results in a minor poleward expansion of the auroral oval on the dusk side, together with a non-negligible widening of the auroral oval both poleward and equatorward on the dawn side, as seen from the maps. As a consequence of the heterogeneous auroral oval expansion depending on MLT sectors, the resulting asymmetry between dawn and dusk in the AOP gets larger as the threshold gets lower. The MLT profiles highlight this variation in the relative dawn-dusk asymmetry: although the overall patterns for all three thresholds are similar, the slope of the line over ∼16–23 MLT slightly increases with an increasing threshold value. We have also tested thresholds greater than $1 \cdot 10^{10}$ eV/cm^2/s/sr (not shown) and found that the dawn-dusk asymmetry in the auroral occurrence oval continues to decrease as the threshold is increased.

We conclude that the AOP spatial variation is stable with respect to the choice of integrated energy flux threshold for positive identification of aurora and that the threshold choice does not influence our study provided that it is roughly in the range of 10^8–10^{10} eV/cm^2/s/sr. However, as shown by the leftmost distribution, a threshold that is too low tends to give noisy results, even if the overall morphology of the auroral occurrence oval shape is unchanged. We therefore suggest that for a threshold to be meaningful, it likely must lie in the interval $5 \cdot 10^8$–10^{10} eV/cm^2/s/sr. We have chosen to use a threshold equal to $2 \cdot 10^9$ eV/cm^2/s/sr, as this value is very similar to the limit chosen by Kilcommons et al. (2017), and has the additional advantage to give a probability of observing aurora in the polar cap closer to zero than the $1 \cdot 10^9$ eV/cm^2/s/sr threshold.

4.4. Response of the AOP to IMF B_y

We now compare the distributions of AOP under different polarities of IMF B_y. Since we combine both hemispheres in our analysis, and since the y component of the IMF is known to affect differently the two hemispheres in terms of ionospheric electrodynamics depending on its sign (Hatch et al., 2022), here we have flipped the sign of B_y in the Southern Hemisphere such that the comparison between the two IMF polarities is valid.

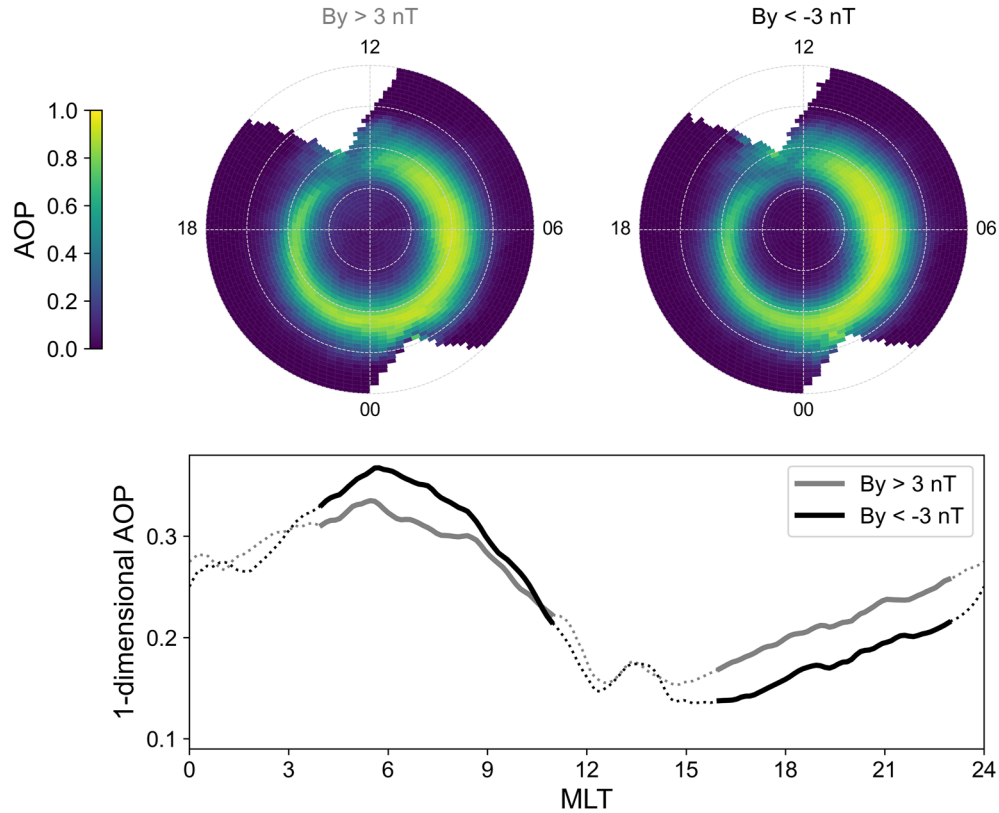

Figure 6. Auroral occurrence probability (AOP) distributions (top row) and magnetic local time profiles of 1D-AOP (bottom panel) for IMF B_y positive (left, gray) and B_y negative (right, black).

The maps in Figure 6 indicate a weak response of the AOP to the sign of B_y. In particular, both distributions vary in a similar fashion, and the usual asymmetry between the dawn and the dusk sides of the auroral oval remains prominent for both orientations of B_y. Nevertheless, the MLT variations of the 1D-AOP highlight a decrease in the dawn-dusk asymmetry for B_y positive.

4.5. Response of the AOP to Substorm Epochs

Figure 7 shows the statistical evolution of the AOP with the substorm cycle, and the corresponding MLT profiles of 1D-AOP, from 30 min before substorm onset ($t = 0$) up until 30 min after onset, separated into 15-min intervals.

We emphasize that a neat interpretation of the substorm influence is difficult when one makes use of a substorm list based on magnetometer data, as the measured geomagnetic variations most likely include the contribution of induced currents (Juusola et al., 2020). Considering solely isolated substorms, as mentioned in Section 2.3, might slightly balance this issue but also results in the exclusion of most of the intense and global events (Rodger et al., 2016). In addition to that, the AOP evolution is automatically smoothed by the choice of time periods for the superposed epoch analysis, as large time ranges mingle the substorm onset times and phases. Finally, we point out that the nightside data are mainly from the Southern Hemisphere (as mentioned in Section 4.2), while the substorms are identified in the north. For all these reasons, the substorm effect on the AOP morphology reported here could be underestimated.

In fact, the first impression from both the maps and MLT profiles is that the AOP is very stable, without any clear correlation with the substorm epoch. A closer look at the midnight region on each map allows us to spot a small widening of the auroral occurrence oval after the substorm onset ($t > 0$). As for the MLT profiles, it can be seen that the after-onset lines (red) are below the before-onset lines (blue) from 3 to 20 MLT, that is, most of the time. However, around the midnight region, which is known to be an MLT sector highly affected by substorm dynamics, the after-onset line slopes increase from 21 to 2 MLT such that the 1D-AOP reaches higher values

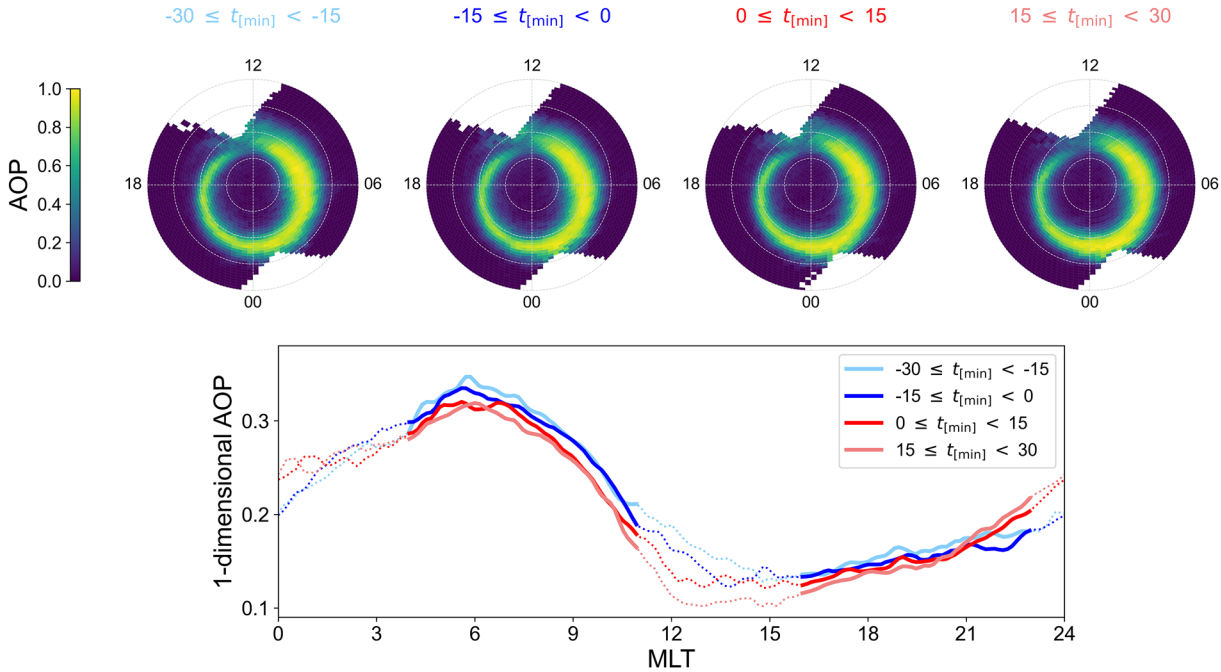

Figure 7. Auroral occurrence probability (AOP) distributions (top row) and magnetic local time profiles of 1D-AOP (bottom panel) for four different 15 min-time ranges around substorm onset. From left to right the time ranges are respectively -30 min $\leq t < -15$ min (light blue), -15 min $\leq t < 0$ min (dark blue), 0 min $\leq t < 15$ min (dark red), 15 min $\leq t < 30$ min (light red).

after substorm onset, compared to before onset. This seems to be in agreement with the increased extent of the auroral occurrence oval after onset observed on the maps. This observation is the only tangible hint that the AOP is not completely uncorrelated to substorm activity, which would be highly unexpected, but such small changes indicate nonetheless that the time scales involved in the AOP dynamics might be longer than what is captured in our substorm analysis.

4.6. Response of the AOP to the Level of Geomagnetic Activity

Here we investigate the response of the AOP to three parameters reflecting either the reconnection rate between the IMF and the magnetosphere (IMF B_z) or the intensity of geomagnetic disturbances (SYM-H and AL indices). Our aim is to make use of those parameters to emulate either a high or a low level of geomagnetic activity and study its influence on the auroral oval dawn-dusk asymmetry.

Figure 8 shows the AOP maps and MLT profiles of the 1D-AOP for the three above-mentioned parameters. For $B_z > 3$ nT, SYM-H > -10 nT and AL > -50 nT (i.e., during low geomagnetic activity, top row), the AOP distributions exhibit a clear preference for the dawn sector (5–10 MLT). The same observation can be made from the MLT profiles with the low activity line (in blue) showing a significant asymmetry between the dawn and dusk sides, with a distinct peak of the 1D-AOP in the dawn sector. On the other hand, for $B_z < -3$ nT, SYM-H < -20 nT and AL < -150 nT (i.e., during high geomagnetic activity, middle row), the AOP dawn preference remains but is less pronounced. For such conditions, the main change in the AOP is an increase in latitudinal extent on the nightside, over approximately 22–5 MLT. From the MLT profiles, the high activity line (in red) shows higher values of the 1D-AOP everywhere in the nightside sector compared to the dayside, with a minor peak in the dawn sector. This results in a less asymmetric pattern in the auroral oval for active times than for quiet times.

In summary, the behavior of the AOP and the associated MLT profiles is stable with regard to the different parameters we investigate. The AOP distributions sorted by B_z, SYM-H and AL all show: (a) an enhanced AOP on the nightside during active periods compared to periods of lower activity, (b) relatively enhanced AOP on the nightside compared to dayside during active times, and (c) a relatively enhanced AOP on the dayside compared to nightside during quiet times. These collateral changes affect the auroral oval extent asymmetry such that the dawn sector is the most prominent during quiet times, while the whole nightside region is predominant over the dayside

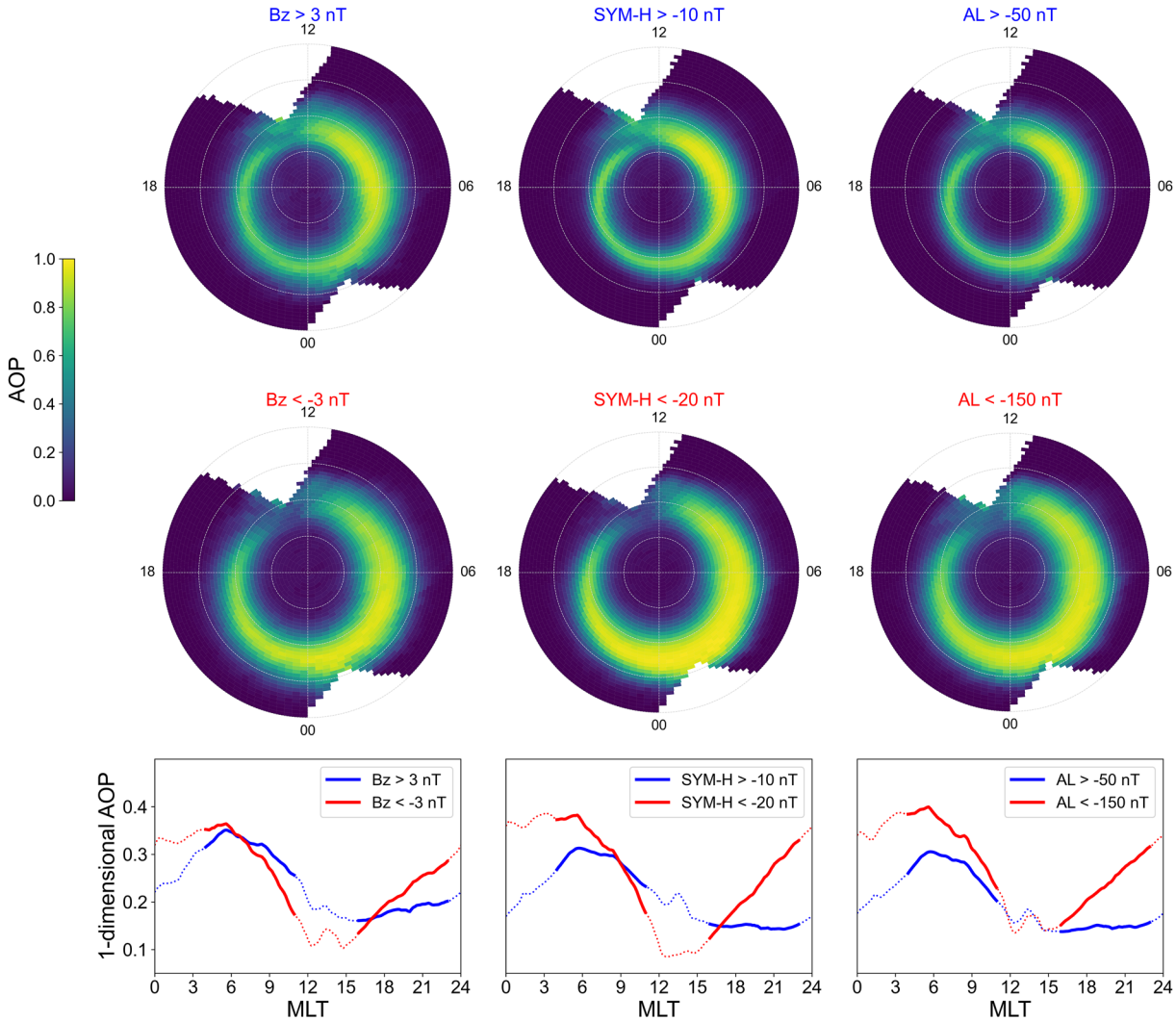

Figure 8. Auroral occurrence probability (AOP) distributions (two top rows) and magnetic local time profiles of 1D-AOP (bottom row) for low (top row, blue) and high (middle row, red) levels of geomagnetic activity, based on different geomagnetic parameters. From left to right the parameters are: IMF B_z, SYM-H index and AL index.

during active times. We conclude that the dawn preference in the auroral oval is influenced by the geomagnetic activity, with an increased dawn-dusk asymmetry as the activity decreases. We discuss this further in Section 5.

5. Discussion

We have investigated the auroral region morphology via the AOP, and have found a persistent dawn-dusk asymmetry in the auroral occurrence oval extent. Such an asymmetric pattern has been observed before in average energy flux studies (e.g., Newell et al., 2009) and explained through the scope of kinetic dynamics. In a detailed review of such studies, Ni et al. (2016) point to the formation of discrete aurora in association with electron acceleration by quasi-static electric fields and dispersive Alfvén waves on the one hand, and to the major role of various magnetospheric waves in driving the diffuse auroral precipitation on the other hand. They also stress that the predominant eastward transport of electrons, leading to a dawn-dusk asymmetry in the auroral oval morphology, is typically interpreted as a result of a combination of $\mathbf{E} \times \mathbf{B}$ and gradient drifting from the nightside plasma sheet.

However, we have shown that the AOP has some specific characteristics (in comparison with the mean energy flux) such as the substantial sensitivity to diffuse precipitation and the overall stability with respect to substorm epochs, as well as solar wind and geomagnetic conditions, suggesting a long-term, large-scale evolution of the AOP morphology. Hence, while we acknowledge the contribution and importance of the mechanisms that

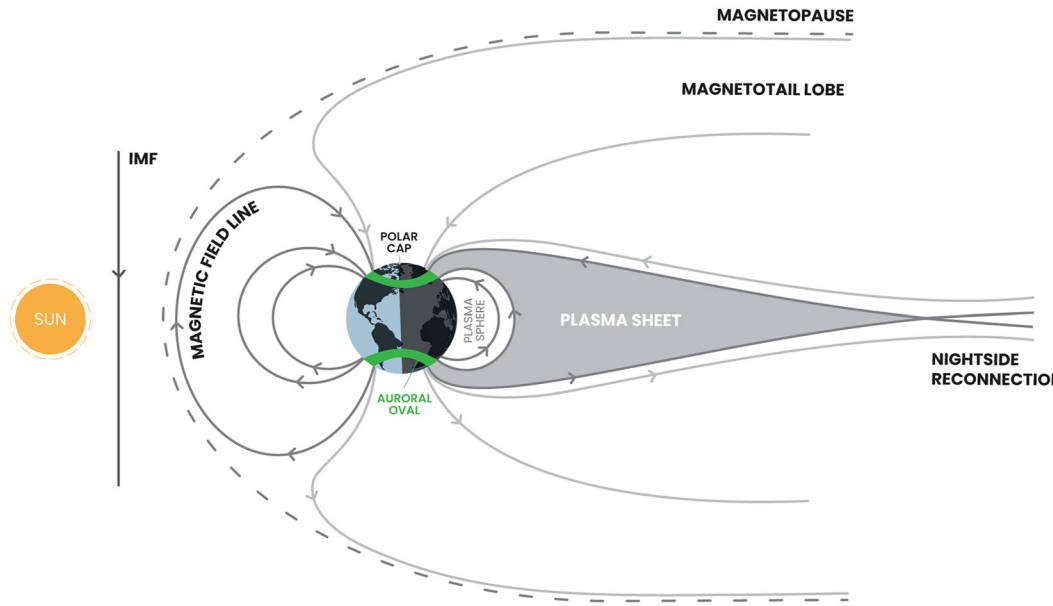

Figure 9. Schematics of the mapping between the auroral oval (in green) and the magnetospheric regions, within the global frame of the open magnetosphere produced by the Dungey cycle. Closed field lines are shown in dark gray, open field lines are in light gray. Illustration not to scale.

traditionally explain the main features of the global distribution of auroral precipitation, we suggest that the AOP is not only affected by the energetic precipitation but also reflects the magnetospheric topology. We thus propose a new interpretation of the observed asymmetry through a fluid description in which the AOP is regulated by the shape and bulk motion of the magnetospheric plasma that maps to the auroral region. This in turn is controlled by the following sequence: plasma sheet production by nightside reconnection (closing of flux), sunward transport, and then loss through dayside reconnection (opening of flux). Given our fluid description, we also suggest that the Earth's corotation, through its influence on the plasma convection pattern, may be partly responsible for the dawn-dusk asymmetry in the auroral occurrence oval. We discuss this in detail below.

5.1. Relation Between AOP and Plasma Sheet Magnetic Flux

The plasma convection pattern around Earth can be explained to first order by the Dungey cycle, which describes the magnetic flux transport in the magnetosphere (Dungey, 1961). More recently the expanding/contracting polar cap (ECPC) paradigm (Cowley & Lockwood, 1992; Milan, 2015), a modern view of the Dungey cycle, has described how convection is excited in relation to reconnection, magnetic flux transport within the magnetosphere, associated polar ionospheric flows, and changes of the polar cap size. Within the ECPC paradigm, the polar cap size, delimited by the open/closed boundary (OCB), reflects the amount of open flux in the magnetotail lobes. Expanding the ECPC concept, the ionospheric projection of the magnetotail plasma sheet (where closed flux is created during reconnection) is thus equatorward of the OCB and is topologically the preferential site of auroral precipitation (Newell et al., 2004).

The distributions shown in Figure 8 indicate that during enhanced geomagnetic activity the latitudinal extent of the AOP increases, especially on the nightside. In addition to that, the latitudinal extent of the AOP is greater on the dayside than on the nightside during geomagnetically quiet intervals. These observations suggest that the AOP evolution follows the sequence of closed magnetic flux production and loss, thus implying a mapping between plasma sheet and auroral oval. Within such a framework, we assume the amount of closed magnetic flux created by nightside reconnection, that is, in the plasma sheet, to be directly related to the probability of observing aurora.

Figure 9 illustrates the open magnetosphere produced by the Dungey cycle and the mapping between the magnetospheric plasma sheet and the auroral oval, in terms of open and closed magnetic field lines (in light and dark gray, respectively). The dayside reconnection between the Earth's and interplanetary magnetic fields comes with an opening of geomagnetic field lines, which are in turn dragged by the solar wind flow to the nightside.

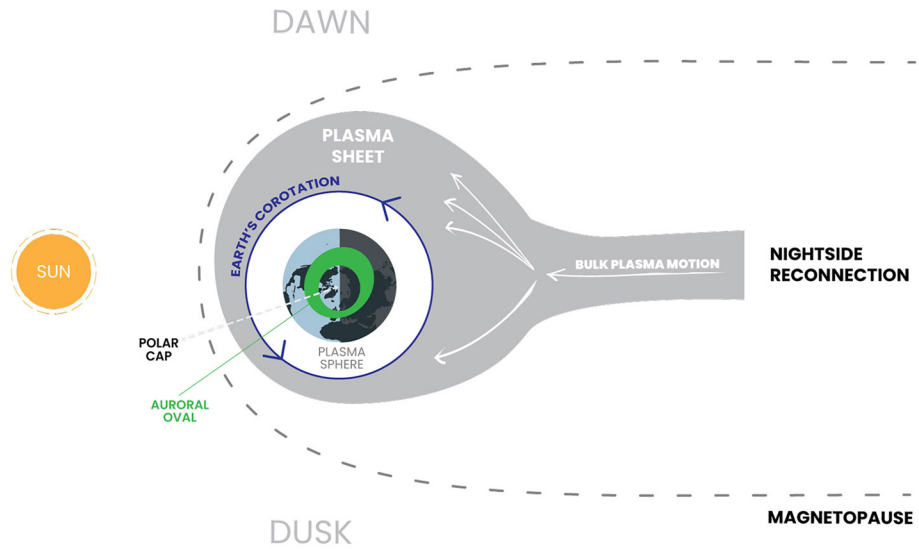

Figure 10. Schematics of the influence of Earth's rotation on the sunward transport of plasma sheet magnetic flux, as seen through a fluid description. Here, the Earth is seen from above the polar region. Illustration not to scale.

This leads to an accumulation of flux and an increase of magnetic pressure in the magnetotail lobes, where the magnetic energy is stored before being released by nightside reconnection between field lines bordering the plasma sheet. The resulting plasma sheet closed field lines are eventually moved around Earth by convection to be destroyed by dayside reconnection, completing the Dungey cycle. In this picture, the auroral oval magnetic footpoints map to the so-called plasma sheet, that is, the magnetospheric boundary between open magnetic field lines in the magnetotail lobes, which map to the polar cap, and the plasmasphere closed field lines, equatorward of the auroral oval.

5.2. Influence of Earth's Rotation on the Convection Pattern

When studying the large-scale plasma circulation in the ionosphere, a correction for the Earth's corotation is generally applied so that an object at a fixed location on Earth has zero velocity. The plasma convection in this corotating frame follows the well-known solar wind-driven two-cell convection pattern (Cowley & Lockwood, 1992), whose dusk cell has been shown to be predominant (Haaland et al., 2007). However, in reality, the high-latitude ionospheric plasma circulation not only reflects the solar wind-driven component but also the rotational motion of Earth. It has been shown that corotation impacts the return flow, making the dawn cell relatively larger than the dusk cell as Earth rotates eastward (Maynard et al., 1995). Additionally, while the solar wind-driven component of the plasma flow is highly dependent on the IMF orientation (intensifying for southward IMF and diminishing for northward IMF), the corotational component only depends on Earth's rotational speed, which is constant in time. This means that the relative importance of the corotational component also varies with the geomagnetic conditions: it tends to be negligible compared to the solar wind-driven component during high geomagnetic activity, while it becomes proportionally more important when the geomagnetic activity is low.

The distributions in Figure 8 show a persistent dawn-dusk asymmetry in the auroral occurrence oval no matter the conditions. Yet, the AOP evinces a clear response to the level of geomagnetic activity with a more distinct preference for the dawn side compared to the dusk side during periods of low activity. This dependence on the level of geomagnetic activity suggests a plausible contribution of the Earth's corotation to the observed dawn-dusk asymmetry since the asymmetric pattern is enhanced during quiet times when corotation gets relatively more significant. Underpinning this argument is the assumption that the plasma sheet maps to the auroral oval, such that the asymmetry in the AOP may be viewed as a consequence of the Earth's rotation through the direct effect of the latter on the plasma sheet magnetic flux transport.

Figure 10 illustrates the circulation of the closed magnetic flux that constitutes the plasma sheet through a fluid description (i.e., we consider only the bulk motion of the plasma). The inner boundary of the plasma sheet delimits the plasmasphere, region of cold, dense, plasma surrounding Earth equatorward of the auroral oval.

It can be seen that after being produced by nightside reconnection in the magnetotail, and as it is transported toward the Earth, the plasma sheet magnetic flux becomes subject to the high-latitude ionospheric convection pattern. During its sunward transport, the plasma sheet magnetic flux is thus under the influence of both the solar wind-driven convection and the Earth's corotation. As we show in what follows, the latter can apparently contribute to a "pile-up" of plasma sheet magnetic flux toward the dawn side, resulting in a wider auroral oval at dawn relative to the oval at dusk. Furthermore, during low geomagnetic activity, the dayside reconnection rate can be so low that the closed magnetic flux is only a little destroyed, resulting in a larger pile-up of flux at dawn, compared to more active periods.

Here we emphasize that the increase of the plasma sheet extent by this pile-up effect is only one interpretation of the influence of Earth's corotation through our fluid description; another possible interpretation could be that the convection of the plasma sheet around Earth goes faster toward dawn because of the corotation. In this alternative interpretation, the plasma sheet magnetic flux would reach the dawn side more often than dusk, which would in turn result in a higher probability of observing aurora at dawn relative to dusk, but not necessarily in a wider auroral oval.

5.3. Theoretical Approach—Model of the Sunward Transport of the 1D-Plasma Sheet Magnetic Flux

In order to test the corotational flow influence in creating the observed dawn-dusk asymmetry in the auroral oval, we construct a simple model of the plasma sheet magnetic flux as a function of magnetic local time. Since we seek a first-order picture of the plasma sheet (PS) fluid dynamics, we make simple assumptions in designing our model. In particular, we choose to consider a 1D, steady-state system. The core parameter is the 1D PS magnetic flux $\Psi(x)$ in units of [Wb/m], with x the length around the circle of latitude λ, starting at 0 MLT; in other words, $\Psi(x)$ can be seen as a magnetic flux per MLT, where MLT is a scaled length between 0 and $2\pi R_E \cos(\lambda)$ (0–24 MLT). We assume this PS magnetic flux to be produced at a rate $P(x)$ [V/m] via magnetic reconnection on the nightside, transported around Earth toward the dayside at a velocity $v(x)$ [m/s] and eventually destroyed via dayside reconnection, in proportion to the available flux, at a rate $\alpha(x)\Psi(x)$ [V/m]. Both $P(x)$ and $\alpha(x)$ are modeled as Gaussian distributions that respectively peak at midnight and noon. The integrated production rate $P(x)$ is chosen so that the total nightside reconnection rate is 30 kV. This corresponds to a total cross polar cap potential of 30 kV, assuming that the dayside and nightside reconnection rates exactly balance. Such value is consistent (same order of magnitude) with typical cross polar cap potential values, as seen for example, in Haaland et al. (2007). On the other hand, the loss coefficient $\alpha(x)$ has an amplitude that is sufficient to destroy all closed flux by dayside reconnection before it reaches noon. The full width at half maximum for both parameters is 1.33 MLT.

The 1D closed magnetic flux $\Psi(x)$ is then described through the time-stationary 1D continuity equation along a circle of latitude λ

$$\Psi(x)\frac{dv(x)}{dx} + v(x)\frac{d\Psi(x)}{dx} = P(x) - \alpha(x)\Psi(x), \tag{1}$$

with $v(x) = V_{SW} + V_{corotation}$ since our model takes into account both solar wind-driven convection flow and constant corotational flow in the sunward transport of the PS magnetic flux. We approximate V_{SW} as $V_0 \sin(x)$, such that it describes a return flow that maximizes at $x = 6$ and 18 MLT. According to convection studies, V_0 is usually between 200 m/s and 600 m/s, depending on the level of geomagnetic activity (Reistad et al., 2018). In our study we make V_0 vary within that range in order to reproduce the balance between corotation and return flow for various geomagnetic conditions. As for the corotation speed $V_{corotation}$, which only varies with geographic latitude, we set it to an approximate value of 158 m/s at 70° MLat (Laundal et al., 2022). By choosing a latitude typically within the auroral region, we ensure that the estimated corotation speed corresponds to its value in the magnetospheric PS.

In the end, all Equation 1 parameters are assumed to be known and only Ψ is an unknown function of x. The transport equation can then be solved by using finite differences with the periodic boundary condition that $\Psi(0) = \Psi(24)$.

5.4. Is Corotation Enough to Explain the Dawn Preference in the AOP ?

We solve Equation 1 for a slow ($V_0 = 200$ m/s) and a fast ($V_0 = 600$ m/s) return flow, and compare the resulting MLT profiles of the modeled PS magnetic flux $\Psi(x)$ for two different corotation/return flow equilibria with the MLT profiles of 1D-AOP for two different levels of geomagnetic activity.

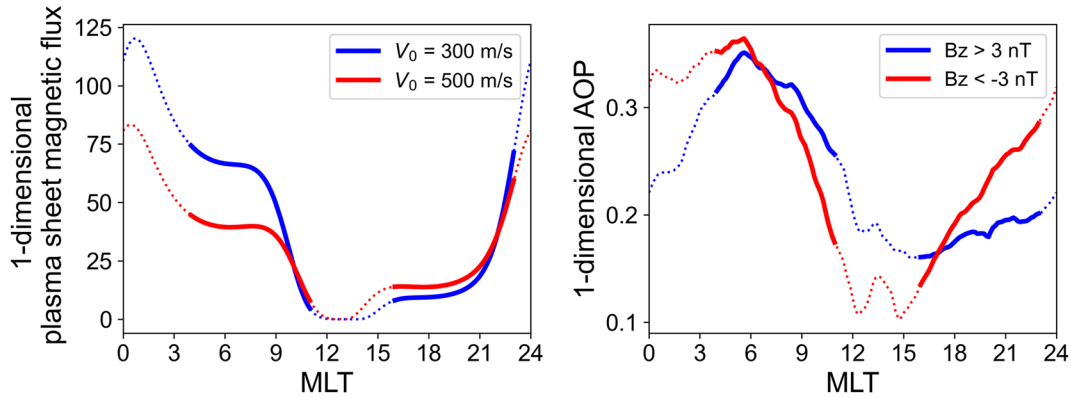

Figure 11. Left panel: Modeled 1D-plasma sheet magnetic flux as a function of magnetic local time (MLT) $\Psi(x)$ for low (blue) and high (red) convection speed. Right panel: 1D-AOP as a function of MLT for B_z positive (blue) and B_z negative (red) (same as the bottom left plot in Figure 8).

The left panel of Figure 11 shows the MLT profiles of the PS magnetic flux derived from our model. As expected from closed flux, and independently of V_0, most of the PS magnetic flux is located on the nightside, with a post-midnight peak, while very little flux is left around noon. Besides that, we can immediately spot the asymmetric distribution of magnetic flux between the dawn and dusk sides. From our investigation of the AOP response to IMF B_z (Section 4.6), we have shown that the MLT profiles of 1D-AOP evince similar features, regardless of B_z sign (right panel of Figure 11). Additionally, Figure 11 highlights how the level of geomagnetic activity influences the dawn-dusk asymmetric pattern for both the 1D-AOP and 1D-PS magnetic flux. Favorable magnetic conditions for reconnection (negative B_z) and increased return flow velocity ($V_0 = 600$ m/s) both express geomagnetically active times, while more quiet times generally come with a northward IMF (positive B_z) and a slower return flow ($V_0 = 200$ m/s). We find that the two quantities show the same specific response, that is an increased asymmetry for lower geomagnetic activity (blue lines) and a reduced, but persistent, asymmetry for higher activity (red lines), with a lingering dawn preference.

The simple model that we have constructed ignores the complexities of several relevant physical processes, including particular mechanisms for particle precipitation and the effects of different solar wind parameters. We nevertheless suggest that the correlation between the 1D-AOP and our model of 1D-PS magnetic flux can be extrapolated such that the asymmetric distributions of PS magnetic flux and AOP are related. In this picture, the role of Earth's corotation in producing a dawn-dusk asymmetry in the auroral occurrence oval thus reflects the driving of more PS magnetic flux toward the dawn side during its sunward transport. The relative importance of the dawn cell compared to the dusk cell is drastically increased during low geomagnetic activity due to the combined action of convection being controlled by corotation and an overall lower rate of removal of accumulated PS flux by dayside reconnection. Conversely, during higher geomagnetic activity the solar wind influence dominates the convection system over corotation, leading to a more homogeneous distribution of PS magnetic flux and a less pronounced dawn preference. Independently of geomagnetic conditions and how intense the corotation effect is, we have argued that this could result in either a magnetic flux pile-up at dawn (wider auroral oval) or simply an increased probability of aurora at dawn, regardless of width.

In conclusion, our fluid description of the evolution of the auroral oval morphology indicates that the Earth's rotation may contribute to the dawn-dusk asymmetry observed in our AOP distributions. Nonetheless, the supposed predominance of the corotation influence on the formation of asymmetric patterns in the auroral oval does not necessarily remain true when going beyond our fluid model and its related bulk plasma motion. When considering the whole complex picture, particle precipitation mechanisms have a central role in producing the observed dawn-dusk asymmetry, and their relative importance compared to the bulk plasma motion associated effects should be thoroughly analyzed. According to (Eq. 3.21 Baumjohann & Treumann, 1997), the magnetic drift speed is proportional to particle energy, such that energetic electrons will drift eastward (and ions westward) faster than the Earth's rotational speed. However, for 1 keV particles, the lower energy limit used for our AOP maps, corotation is faster than magnetic drift by a factor of ≈6.7, assuming a dipole field at 67° latitude. This supports our suggestion that corotation influences the dawn-dusk asymmetry observed in this paper, although it is likely negligible for higher energy particles.

6. Conclusion

In this study, we have presented a method for investigating the auroral oval morphology. Using a threshold for aurora detection of $2 \cdot 10^9$ eV/cm^2/s/sr, we have derived the AOP from 20 years of DMSP/SSJ electron energy flux measurements in the energy range 1–30 keV, and have used it to assess the probabilistic extent of the auroral oval as a function of magnetic local time. We have shown that the AOP evinces a typical asymmetric pattern with a clear and persistent enhancement at dawn that is independent of the data selection. In particular, this pattern is very well conserved with respect to variation of the auroral detection threshold as well as substorm epoch. On the other hand, the dawn-dusk asymmetry varies with the level of geomagnetic activity, being more pronounced during geomagnetically quiet periods and less prominent during periods of enhanced geomagnetic activity. While this dawn-dusk asymmetry in the auroral oval has been described before in average auroral precipitation studies, here we have pointed out the differences between the AOP and the average energy flux, and the prominence of diffuse precipitation in our data analysis.

These aspects, taken together, prompt consideration of possible alternatives to the usual explanation of the auroral oval dynamics through kinetic effects. In specific, we have posited that it may be possible to describe the governing physical processes involved in shaping the asymmetric auroral oval in terms of convection by assuming a mapping between the magnetospheric plasma sheet and the auroral oval. We have therefore constructed a simple 1-D model of the plasma sheet magnetic flux, subject to production and loss of closed flux by magnetic reconnection as well as Earth's corotation, to compare its MLT dependence with that of the AOP. Our model suggests that the features of the auroral occurrence oval may depend on the amount of plasma sheet magnetic flux being convected from the nightside to the dayside. Moreover, the persistent dawn preference can apparently be described in part as a consequence of the Earth's rotation, which drives more magnetic flux toward the east. The tendency of the dawn-dusk asymmetry to be more prominent during low geomagnetic activity supports the idea that corotation plays a role in shaping the distribution of the occurrence of aurora.

For future research, it will be of interest to extend the database that we use in this study by including precipitation measurements made by other low Earth-orbiting satellites, such as the NOAA POES satellites, or possibly combining precipitation measurements with, for example, global auroral images from the upcoming SMILE mission. One could also make use of magnetohydrodynamics simulations to produce model AOP distributions.

Data Availability Statement

The data used in this paper (see Section 2) come from publicly available databases through the following links. The DMSP/SSJ data were obtained from NASA/GSFC CDAWeb at https://cdaweb.gsfc.nasa.gov/pub/data/dmsp/. The OMNI data, including the solar wind data and geomagnetic activity indices, are available on the NASA/GSFC SPDF interface at http://spdf.gsfc.nasa.gov/pub/data/omni/high_res_omni/. The substorm data are accessible at the JHU/APL SuperMAG website at https://supermag.jhuapl.edu/substorms/?tab=download.

Acknowledgments
This study was funded by the Trond Mohn Foundation, and by the Research Council of Norway through contracts 223252/F50 and 300844/F50. We thank R.J. Redmon and L.M. Kilcommons for providing the DMSP/SSJ data, and J.H. King and N.E. Papitashvili for the multi-sources OMNI data. We acknowledge the use of NASA/GSFC SPDF service to obtain these data. We also acknowledge the substorm timing list identified by the Ohtani and Gjerloev technique (Ohtani & Gjerloev, 2020), the SMU and SML indices (Newell & Gjerloev, 2011); and the SuperMAG collaboration (Gjerloev, 2012). Finally, we thank A. Decotte for nicely illustrating the conceptual ideas behind this paper (Figures 9 and 10).

References

Baumjohann, W., & Treumann, R. (1997). *Basic space plasma physics*. Imperial College Press.

Breddels, M. A., & Veljanoski, J. (2018). Vaex: Big data exploration in the era of gaia. *A&A*, *618*, A13. https://doi.org/10.1051/0004-6361/201732493

Burrell, A. G., Chisham, G., Milan, S. E., Kilcommons, L., Chen, Y.-J., Thomas, E. G., & Anderson, B. (2020). Ampere polar cap boundaries. *Annales Geophysicae*, *38*(2), 481–490. https://doi.org/10.5194/angeo-38-481-2020

Chisham, G., Burrell, A. G., Thomas, E. G., & Chen, Y.-J. (2022). Ionospheric boundaries derived from auroral images. *Journal of Geophysical Research: Space Physics*, *127*(7). e2022JA030622. https://doi.org/10.1029/2022JA030622

Coumans, V., Gérard, J.-C., Hubert, B., & Evans, D. S. (2002). Electron and proton excitation of the FUV aurora: Simultaneous image and NOAA observations. *Journal of Geophysical Research*, *107*(A11), 1347. https://doi.org/10.1029/2001JA009233

Cowley, S. (1981). Magnetospheric asymmetries associated with the y-component of the IMF. *Planetary and Space Science*, *29*(1), 79–96. https://doi.org/10.1016/0032-0633(81)90141-0

Cowley, S., & Lockwood, M. (1992). Excitation and decay of solar-wind driven flows in the magnetosphere-ionosphere system. *Annales Geophysicae*, *10*, 103–115.

Di Matteo, S., & Sivadas, N. (2022). Solar-wind/magnetosphere coupling: Understand uncertainties in upstream conditions. *Frontiers in Astronomy and Space Sciences*, *9*. https://doi.org/10.3389/fspas.2022.1060072

Dombeck, J., Cattell, C., Prasad, N., Meeker, E., Hanson, E., & McFadden, J. (2018). Identification of auroral electron precipitation mechanism combinations and their relationships to net downgoing energy and number flux. *Journal of Geophysical Research: Space Physics*, *123*(12). 2018JA025749. https://doi.org/10.1029/2018JA025749

Dungey, J. W. (1961). Interplanetary magnetic field and the auroral zones. *Physical Review Letters*, *6*(2), 47–48. https://doi.org/10.1103/PhysRevLett.6.47

Feldstein, Y. (2016). The discovery and the first studies of the auroral oval: A review. *Geomagnetism and Aeronomy*, *56*(2), 129–142. https://doi.org/10.1134/S0016793216020043

Feldstein, Y. I. (1964). Auroral morphology, II. Auroral and geomagnetic disturbances. *Tellus*, *16*(2), 258–267. https://doi.org/10.1111/j.2153-3490.1964.tb00164.x

Feldstein, Y. I., & Starkov, G. V. (1967). Dynamics of auroral belt and polar geomagnetic disturbances. *Planetary and Space Science*, *15*(2), 209–229. https://doi.org/10.1016/0032-0633(67)90190-0

Gjerloev, J. W. (2012). The SuperMAG data processing technique. *Journal of Geophysical Research: Space Physics*, *117*(A9). https://doi.org/10.1029/2012JA0176

Haaland, S., Paschmann, G., Foerster, M., Quinn, J., Torbert, R., Mcilwain, C., et al. (2007). High-latitude plasma convection from cluster EDI measurements: Method and IMF-dependence. *Annales Geophysicae*, *25*(1), 239–253. https://doi.org/10.5194/angeo-25-239-2007

Hardy, D. A., Gussenhoven, M. S., & Holeman, E. (1985). A statistical model of auroral electron precipitation. *Journal of Geophysical Research*, *90*(A5), 4229–4248. https://doi.org/10.1029/JA090iA05p04229

Hatch, S. M., Laundal, K. M., & Reistad, J. P. (2022). Testing the mirror symmetry of birkeland and ionospheric currents with respect to magnetic latitude, dipole tilt angle, and imf by. *Frontiers in Astronomy and Space Sciences*, *9*. https://doi.org/10.3389/fspas.2022.958977

Holzworth, R. H., & Meng, C.-I. (1975). Mathematical representation of the auroral oval. *Geophysical Research Letters*, *2*(9), 377–380. https://doi.org/10.1029/GL002i009p00377

Juusola, L., Vanhamäki, H., Viljanen, A., & Smirnov, M. (2020). Induced currents due to 3d ground conductivity play a major role in the interpretation of geomagnetic variations. *Annales Geophysicae*, *38*(5), 983–998. https://doi.org/10.5194/angeo-38-983-2020

Keiling, A., Wygant, J. R., Cattell, C. A., Mozer, F. S., & Russell, C. T. (2003). The global morphology of wave Poynting flux: Powering the aurora. *Science*, *299*(5605), 383–386. https://doi.org/10.1126/science.1080073

Khazanov, G. V., & Glocer, A. (2020). How magnetically conjugate atmospheres and the magnetosphere participate in the formation of low-energy electron precipitation in the region of diffuse aurora. *Journal of Geophysical Research: Space Physics*, *125*(8). https://doi.org/10.1029/2020JA028057

Kilcommons, L. M., Redmon, R. J., & Knipp, D. J. (2017). A new DMSP magnetometer and auroral boundary data set and estimates of field-aligned currents in dynamic auroral boundary coordinates. *Journal of Geophysical Research: Space Physics*, *122*(8), 9068–9079. https://doi.org/10.1002/2016JA023342

King, J. H., & Papitashvili, N. E. (2005). Solar wind spatial scales in and comparisons of hourly wind and ace plasma and magnetic field data. *Journal of Geophysical Research*, *110*(A2), A02104. https://doi.org/10.1029/2004JA010649

Laundal, K. M., Madelaire, M., Ohma, A., Reistad, J., & Hatch, S. (2022). The relationship between interhemispheric asymmetries in polar ionospheric convection and the magnetic field line footpoint displacement field. *Frontiers in Astronomy and Space Sciences*, *9*. https://doi.org/10.3389/fspas.2022.957223

Laundal, K. M., Østgaard, N., Frey, H. U., & Weygand, J. M. (2010). Seasonal and interplanetary magnetic field–dependent polar cap contraction during substorm expansion phase. *Journal of Geophysical Research*, *115*(A11). https://doi.org/10.1029/2010JA015910

Maynard, N. C., Denig, W. F., & Burke, W. J. (1995). Mapping ionospheric convection patterns to the magnetosphere. *Journal of Geophysical Research*, *100*(A2), 1713–1721. https://doi.org/10.1029/94JA02626

Milan, S. E. (2015). Sun et lumière: Solar wind-magnetosphere coupling as deduced from ionospheric flows and polar auroras. In S. W. H. Cowley FRS, D. Southwood, & S. Mitton (Eds.), *Magnetospheric plasma physics: The impact of jim dungey's research* (pp. 33–64). Springer International Publishing.

Milan, S. E., Lester, M., Cowley, S. W. H., Oksavik, K., Brittnacher, M., Greenwald, R. A., et al. (2003). Variations in the polar cap area during two substorm cycles. *Annales Geophysicae*, *21*(5), 1121–1140. https://doi.org/10.5194/angeo-21-1121-2003

Moore, T. E., Chandler, M. O., Chappell, C. R., Pollock, C. J., Waite, J. H., Horwitz, J. L., et al. (1989). Features of terrestrial plasma transport [and discussion]. *Philosophical Transactions of the Royal Society of London - Series A: Mathematical and Physical Sciences*, *328*(1598), 235–254.

Newell, P. T., Feldstein, Y. I., Galperin, Y. I., & Meng, C.-I. (1996). Morphology of nightside precipitation. *Journal of Geophysical Research*, *101*(A5), 10737–10748. https://doi.org/10.1029/95JA03516

Newell, P. T., & Gjerloev, J. W. (2011). Evaluation of SuperMAG auroral electrojet indices as indicators of substorms and auroral power. *Journal of Geophysical Research: Space Physics*, *116*(A12). https://doi.org/10.1029/2011JA016779

Newell, P. T., Liou, K., Zhang, Y., Sotirelis, T., Paxton, L. J., & Mitchell, E. J. (2014). Ovation prime-2013: Extension of auroral precipitation model to higher disturbance levels. *Space Weather*, *12*(6), 368–379. https://doi.org/10.1002/2014SW001056

Newell, P. T., Ruohoniemi, J. M., & Meng, C.-I. (2004). Maps of precipitation by source region, binned by imf, with inertial convection streamlines. *Journal of Geophysical Research*, *109*(A10), A10206. https://doi.org/10.1029/2004JA010499

Newell, P. T., Sotirelis, T., & Wing, S. (2009). Diffuse, monoenergetic, and broadband aurora: The global precipitation budget. *Journal of Geophysical Research*, *114*(A9). https://doi.org/10.1029/2009JA014326

Ni, B., Thorne, R., Zhang, X.-J., Bortnik, J., Pu, Z., Xie, L., et al. (2016). Origins of the earth's diffuse auroral precipitation. *Space Science Reviews*, *200*(1–4), 205–259. https://doi.org/10.1007/s11214-016-0234-7

Ohtani, S., & Gjerloev, J. W. (2020). Is the substorm current wedge an ensemble of wedgelets?: Revisit to midlatitude positive bays. *Journal of Geophysical Research: Space Physics*, *125*(9). https://doi.org/10.1029/2020JA027902

Papitashvili, N., Bilitza, D., & King, J. (2014). OMNI: A description of near-earth solar wind environment. *40th cospar scientific assembly*, (Vol. 40, p. C0.1-12-14).

Redmon, R. J., Denig, W. F., Kilcommons, L. M., & Knipp, D. J. (2017). New DMSP database of precipitating auroral electrons and ions. *Journal of Geophysical Research: Space Physics*, *122*(8), 9056–9067. https://doi.org/10.1002/2016JA023339

Reistad, J. P., Østgaard, N., Laundal, K. M., Ohma, A., Snekvik, K., Tenfjord, P., et al. (2018). Observations of asymmetries in ionospheric return flow during different levels of geomagnetic activity. *Journal of Geophysical Research: Space Physics*, *123*(6), 4638–4651. https://doi.org/10.1029/2017JA025051

Richmond, A. D. (1995). Ionospheric electrodynamics using magnetic apex coordinates. *Journal of Geomagnetism and Geoelectricity*, *47*(2), 191–212. https://doi.org/10.5636/jgg.47.191

Rodger, C. J., Cresswell-Moorcock, K., & Clilverd, M. A. (2016). Nature's grand experiment: Linkage between magnetospheric convection and the radiation belts. *Journal of Geophysical Research: Space Physics*, *121*(1), 171–189. https://doi.org/10.1002/2015JA021537

Shue, J.-H., Newell, P. T., Liou, K., & Meng, C.-I. (2001). Influence of interplanetary magnetic field on global auroral patterns. *Journal of Geophysical Research*, *106*(A4), 5913–5926. https://doi.org/10.1029/2000JA003010

Tromholt, S. (1882). *Om nordlysets perioder/sur les périodes de l'aurore boréale, l'annuaire 1880*. Inst. Météorol. Danois.